The Timescale of Plume-Driven Recratonization: A Complete Record from the Tarim Basin, Northwest China

Yin Liu[1,3 *†], Yiduo Liu[2,3 *†], John Suppe[3], Yingchang Cao[1], Fang Hao[1], Kongyou Wu[1], and Zicheng Cao[4]

[1] Key Laboratory of Deep Oil and Gas, School of Geosciences, China University of Petroleum (East China), Qingdao, Shandong 266580, China

[2] Institute of Mountain Hazards and Environment, Chinese Academy of Sciences, Chengdu, Sichuan 610041, China

[3] Department of Earth and Atmospheric Sciences, University of Houston, Houston, TX 77204-5007, USA

[4] Exploration and Development Research Institute, SINOPEC Northwest Oilfield Branch, Urumqi, Xinjiang 830011, China

[*] Corresponding authors: Yin Liu (liuyin@upc.edu.cn), Yiduo Liu (liuyiduo@imde.ac.cn)

†These authors contributed equally to this work.

Key Points:

- We apply fault-related folding theory-based seismic interpretation and area-depth analysis to study the faults in central Tarim Basin.
- Two episodes of transpressional deformation are fiybd: Earliest Ordovician to Devonian, and the entire Mesozoic.
- Mesozoic strains indicate protracted adjustment after the Permian plume, marking a timescale of ~200 Myr for plume-driven recratonization.

Abstract

How fast a plume can stitch two cratonic nuclei into a stable one remains under-investigated. The Tarim continental block in central Asia is recratonized by a Permian-aged plume and preserves a complete record before, during, and after the plume-driven recratonization. Here we conduct area-depth analysis on seismic reflection data from the central Tarim Basin to date the Phanerozoic deformation. All thrusts and strike-slip faults investigated underwent an early deformation stage (Earliest Ordovician-Middle Devonian), a hiatus stage (Late Devonian-Late Permian), and a newly-discovered deformation stage throughout the Mesozoic. Both deformation stages within Tarim are driven by the subduction and accretion surrounding the block. The Mesozoic finite strains highlight the continuous adjustment as the plume-welded continental lithosphere heals and strengthens. The Tarim plume-driven recratonization concludes not immediately, but ~200 Myr after the plume activity ceased, establishing a characteristic timescale for such events in Earth's history.

Plain Language Summary

Mantle plumes can either weaken or strengthen continental lithosphere. While the weakening effect is well-documented, the strengthening process is rare. In such a process called recratonization, a mantle plume feeds into a thin spot of stretched lithosphere and stitch it back together to form a stable craton. To better understand how fast such a stitch heals, we examine the Tarim block in Northwest China which is stitched by a Permian-aged plume and preserves a complete record before, during, and after the plume-driven recratonization. We apply area-depth method in seismic interpretation to study the structures and stratigraphy in the central Tarim Basin. All thrusts and strike-slip faults there undergo two deformation stages coevally: Earliest Ordovician–Middle Devonian, and the Mesozoic. They are caused by the plate convergence surrounding the Tarim in Paleo- and Mesozoic. Our finding refines the onset time and tectonic configuration of the Early-Paleozoic deformation. More importantly, the newly-discovered Mesozoic strains demonstrate protracted internal adjustment to far-field compression as the plume-welded lithosphere solidifies and strengthens. The cessation of intra-Tarim deformation by the end of Mesozoic marks the completion of plume-driven recratonization, not immediately, but ~200 Myr after the plume activity ceased.

1 Introduction

Continental lithosphere can be modified, either constructively or destructively, by subducting plates and rising plumes (Lee et al., 2011; Pearson et al., 2021). Among these tectonic processes, a less documented scenario is plume-driven recratonization, in which mantle plume-derived melt residues feed into a thin lithospheric trap between two cratonic nuclei and weld them together to form a stable craton (Liu et al., 2021a). While such processes have been studied via igneous records and numerical simulations (Liu et al., 2021; Xu et al., 2023), a fundamental aspect -- the timescale for a plume to fully unite two cratonic nuclei into one -- remains under-investigated in geological records.

The Tarim Basin in central Asia (Fig. 1) offers an opportunity to constrain the timescale of plume-driven recratonization. The Tarim block that underlies the basin behaves as a rigid, craton-like continent during the Cenozoic Himalaya-Tibetan orogeny (Avouac & Tapponnier, 1993; Yin & Nie, 1996). Nevertheless, it did not obtain the cratonic nature in Precambrian like many other cratons did (Pearson et al., 2021). Instead, the two cratonic nuclei, i.e., North Tarim, and South Tarim, evolved individually in Archean, amalgamated in Proterozoic along the Central Tarim suture zone (Guo et al., 2005; Xu et al., 2013; Yang et al., 2018; Zhao et al., 2021), and accommodated significant shortening during the Paleozoic (Carroll et al., 1995; Qiu et al., 2019; Yin & Nie, 1996). The Tarim finally became a coherent, stable craton after the emplacement of the Permian (ca. 300-270 Ma) plume-derived large igneous province (LIP) (Xu et al., 2014; Zhang et al., 2010a; Xu et al., 2020). Its lithosphere is thick (>200 km) at present (Koulakov, 2011), but was thinner (<150 km) in Permian (Xu et al., 2014). Therefore, regardless of the debates on whether and when the Tarim had cratonized in Precambrian (Yin & Nie, 1996; Zhao et al., 2021), for its Phanerozoic evolution, its lithosphere must have been thickened, strengthened, and recratonized by the Permian plume, making it the youngest known case of plume-driven recratonization (Xu et al., 2023).

The Tarim basin preserves a relatively complete sedimentary record from Neoproterozoic to Cenozoic and hinders a direct sampling of basement rocks to study the recratonization. On the other hand, the cover sequences could carry information before, during, and after the recratonization. Previous studies suggest that the Early-Paleozoic deformation in central Tarim initiated in the latest Middle Ordovician, terminated in Devonian, and did not recur afterward; its tectonic origin is attributed to the progressive suturing of the Proto-Tethyan Oceans along the southern Tarim margin (Qiu et al., 2019). These insights are inferred from qualitative interpretation of seismic reflection profiles. Note, however, that it is naturally challenging to pinpoint the shortening strains at sub-seismic resolution, particularly at the beginning or waning stage of deformation (Schlische et al., 2014). Considering the complex tectonic history of Tarim and the surrounding regions in Asia (Cocks & Torsvik, 2013; Yin & Harrison, 2000), the lifespan and episode of the finite-strain deformation pre- and post-Permian plume event could be underestimated, or even overlooked.

We hypothesize that the Tarim lithosphere did not recratonize immediately after the Permian plume event, and the interior Tarim lithosphere could still deform as the plume-derived melts were solidifying. Deformation, and the absence of it, in sedimentary sequences can be used to indicate lithospheric tectonics. We use two- (2-D) and three-dimensional (3-D) seismic reflection data to analyze the structures and stratigraphy in central Tarim Basin. We adopt fault-related folding theory in seismic interpretation (Shaw et al., 2005; Suppe, 1983). Then, we perform area-depth analysis to quantify the timing of deformation and syn-kinematic deposition (Epard & Groshong, 1993; Gonzalez-Mieres & Suppe, 2011). Placing our results in a regional context allows us to better understand the Phanerozoic deformation and recratonization of Tarim.

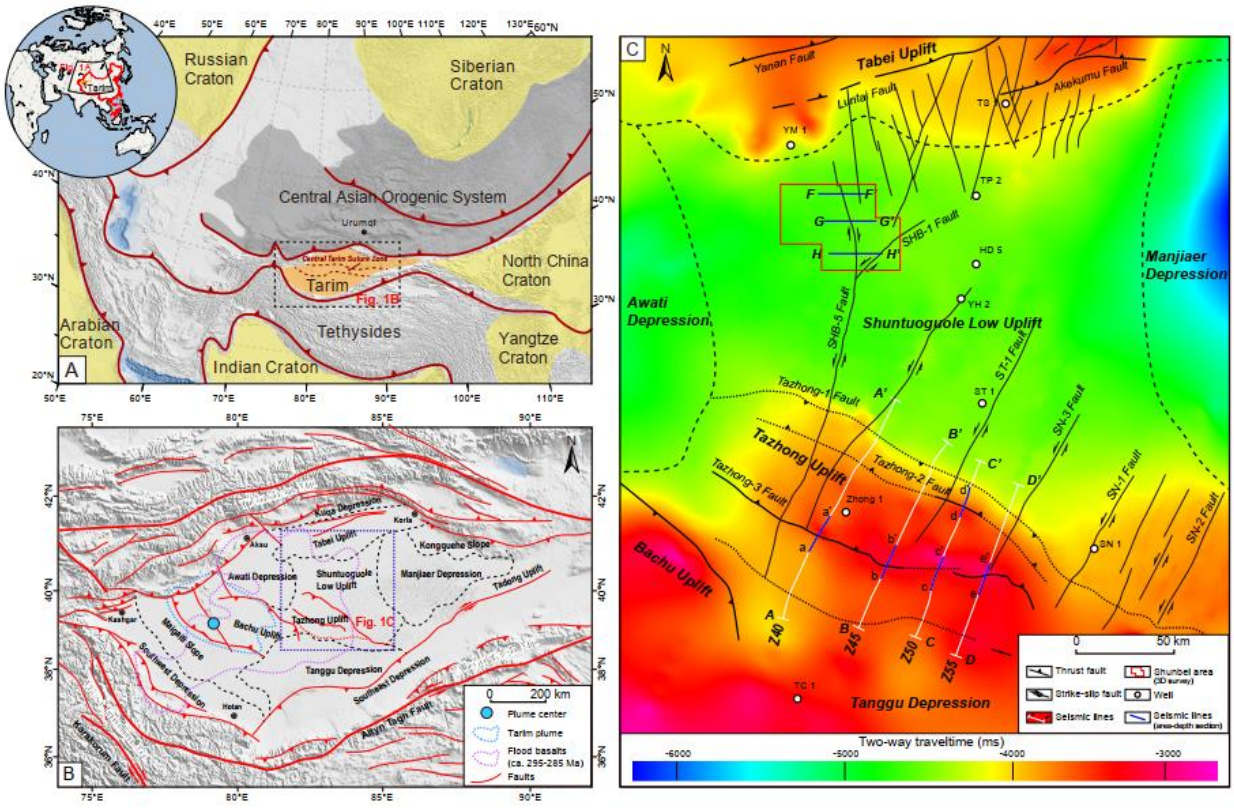

Fig. 1. Location and geological background. (A) Tectonic map of Tarim block and surrounding regions. (B) Topography, major faults, and tectonic units in Tarim. (C) Fault systems in Tazhong-Shunbei. Base map shows the depth (in two-way traveltime) of top Middle Ordovician. White line denotes the 2-D seismic lines in Figs. 2A and S1. Red polygon marks the horizon slices in Figs. 2C and S3. Blue line marks the eight sections for area-depth analysis.

2 Geological Setting

The Tarim Block is an amalgamated craton (Fig. 1A) bounded by the Western Kunlun, Altyn Tagh, and Tian Shan orogenic belts due to the opening and consumption of the Paleo-Asian and the Tethyan Oceans to the north and south, respectively (Xiao et al., 2002; Yin & Harrison, 2000). It shows rigid, craton-like behavior in Cenozoic (Avouac & Tapponnier, 1993; Xu et al., 2020). An east-trending high aerial magnetic anomaly lies across central Tarim, implying an ocean basin that once separated, and then sutured, the North and South Tarim blocks in Precambrian (Xu et al., 2013; Zhao et al., 2021). This suture is reactivated as an intra-continental orogen in Early Paleozoic (Qiu et al., 2019; Yin & Nie, 1996). The Tarim LIP was emplaced episodically in Permian (~300-270 Ma) (Xu et al., 2014; Zhang et al., 2010), and strengthened the Tarim lithosphere (Xu et al., 2020, 2023).

The Tarim Basin consists of twelve tectonostratigraphic units (uplifts, depressions, and slopes) (Fig. 1B). Our study area is the Tazhong Uplift and the Northern Shuntuoguole Low Uplift (a.k.a. “Shunbei”) in central Tarim. This area is ~200 km from the eruption center of the Tarim LIP (Fig. 1B), and flood basalts and sill intrusions are present here (Yao et al., 2018).

Thrust and strike-slip fault systems are found in the Paleozoic (Fig. 1C) (Deng et al., 2019; Liu et al., 2023). The Tazhong Uplift is bounded by NWW-striking thrust faults. They are cut by strike-slip fault arrays, which extend northward to the Shuntuoguole and Tabei Uplifts (Deng et al., 2019; Liu et al., 2023). The central Tarim Basin preserves a broadly complete strata from Neoproterozoic to Cenozoic, whose total thickness exceeds 10 km. Conventionally, twenty reflectors, named as "T_i^j", are used in seismic interpretation, representing key seismic stratigraphic boundaries (Fig. S1).

3 Materials and Methods

3.1 Data

We use 2-D seismic lines from the Tazhong Uplift and horizontal and vertical slices from high-resolution 3-D seismic surveys in Shunbei for seismic interpretation (Fig. 1C) (Supplementary Materials).

3.2 Seismic interpretation

Seismic interpretation is conducted on two-way traveltime sections based on fault-related folding theory (Shaw et al., 2005; Suppe, 1983; Suppe & Medwedeff, 1990). We interpret key reflectors, unconformities, fault traces, fold axial surfaces, and growth strata (Suppe et al., 1992; Vergés et al., 2002).

3.3 Area-depth analysis

We adopt the area-depth method on depth sections to distinguish the syn-tectonic (growth) strata from the non-tectonic (pregrowth and no-growth) strata (Epard & Groshong, 1993; Groshong & Epard, 1994; Gonzalez-Mieres & Suppe, 2006; 2011). This method is developed for fold-and-thrust structures; here we also apply it to strike-slip faulting (Fig. S2). On the obtained area-depth graphs, we identify the pregrowth and growth stages, infer the detachment's depth, and constrain the timing of deformation (refer to Supplementary Materials for details).

4. Results

4.1 Tazhong

The Tazhong Uplift is cored by a large, broad anticline with thrust faults and is overlain by Paleozoic-Cenozoic strata (Fig. 1C). We interpret two southwest-verging thrusts within Lower Paleozoic (below T_6^0) (Figs. 2A, S3). The Tazhong-3 thrust exhibits ramp-flat geometry and develops fault-bend and fault-propagation folds. It soles into a detachment in or around the evaporite-bearing Middle Cambrian Awatage Formation (T_8^1). To the northeast, the Tazhong-2

thrust cuts Cambrian-Ordovician and soles into the same shallow detachment. Northeastward, this fault can be traced further down-dip (at or below T_9^0) based on the shear fault-bend fold geometry (Suppe et al., 2004) in T_8^0-T_9^0 reflectors. Both faults and their related folds show along-strike geometric variations.

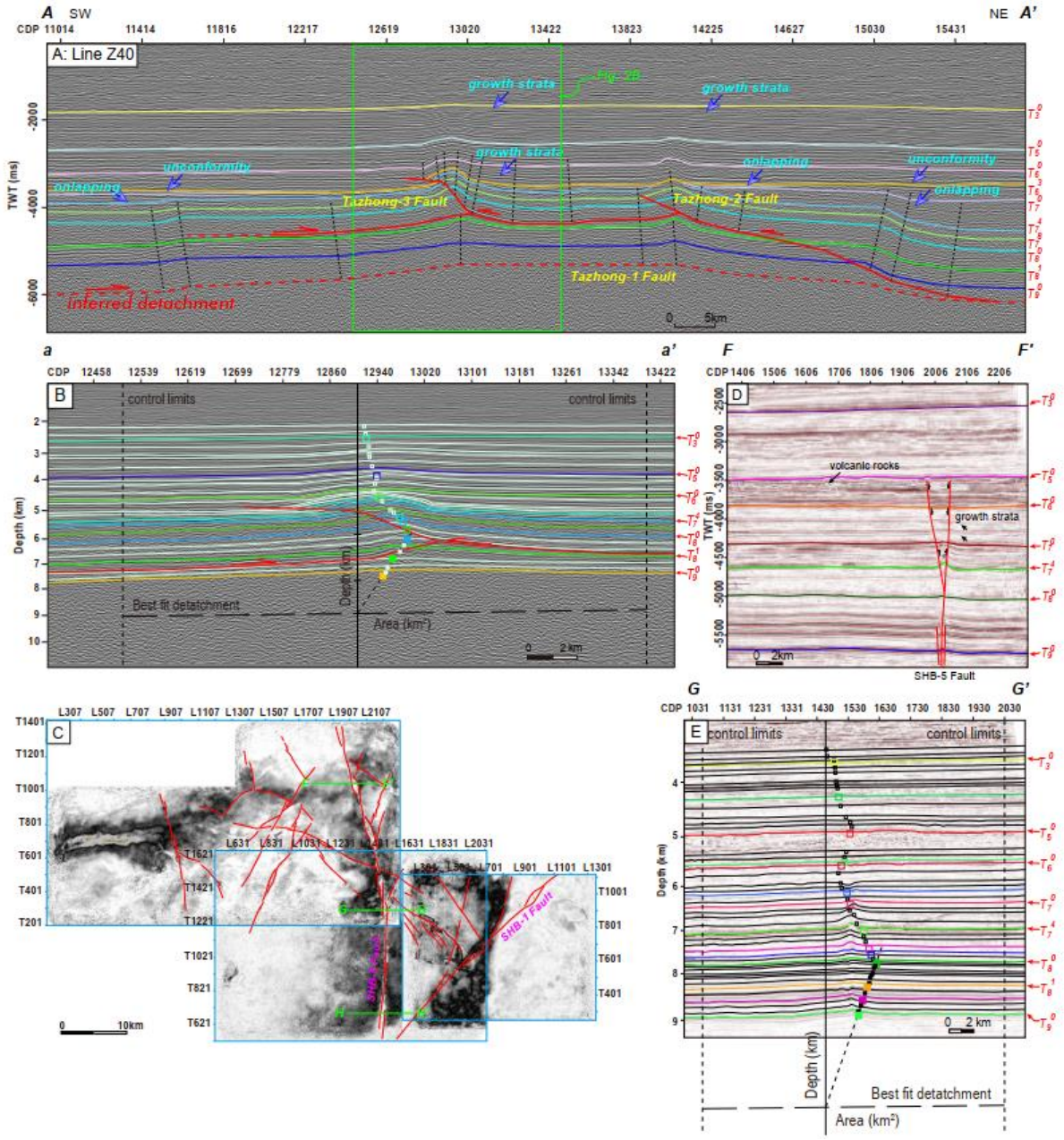

Fig. 2. Seismic interpretation results and area-depth analyses. (A) Interpreted 2-D seismic profile A-A' on Line Z40 across Tazhong Uplift. Horizontal axis is common-depth-point. Vertical axis is two-way traveltime. Vertical exaggeration: ~3 times. (B) Area-depth analysis on depth-domain section a-a' within profile A-A'. (C) Horizontal slice of reflectors T74 (top Middle Ordovician) in Shunbei. (D) Interpreted profile G-G' across SHB-5 fault in Shunbei. Vertical exaggeration: ~3.5 times. (E) Area-depth analysis on depth-domain profile G-G'. See Fig. 1C for locations.

Cambrian to Middle Ordovician (T_9^0-T_7^4) strata possess a broadly constant thickness and continuous seismic reflectors. Unconformities are present at or near the top Ordovician (T_7^0), Silurian (T_6^3), and top Middle Devonian (T_6^0) (Figs. 2A, S3). We recognize two sets of growth strata: Middle Ordovician to Lower Carboniferous (T_7^4 to T_6^0 and above), and Mesozoic (above T_5^0 to ~T_3^0), based on limb rotation, onlapping deposition, and thickness variation (Shaw et al., 2005). The former one has been documented (Qiu et al., 2019; Yin & Nie, 1996), whereas the latter is newly recognized and requires validation.

Kink bands are found in Neoproterozoic-Ordovician outside the Tazhong-2 and Tazhong-3 fold-and-thrust structures. Therefore, a deeper detachment fault must exist. These two detachments form a structural wedge under Tazhong Uplift. The overall structure can be depicted as an open-system detachment fold (Suppe, 2011) that consists of a basal detachment in Precambrian, a roof detachment in Cambrian, and two roof ramp thrusts.

We select five sections across the Tazhong Uplift (blue lines in Fig. 1C and green boxes in Figs. 2A, S3) and apply the area-depth method. In section a-a', the basal detachment is at ~9 km depth (Fig. 2B). Eastward, it gradually deepens to 9.5 km (b-b'), 10.0 km (c-c'), and 10.2 km (d-d', e-e') (Fig. S4).

4.2 Shunbei

Strike-slip faults dominate the Shunbei area. Their structures vary with depths (Figs. 2C, 2D, S5). On horizon T_7^4 (top Middle Ordovician), the north-trending SHB-5 fault is dextral-slip and consists of left-step, *en échelon* segments (Fig. 2C). Small, elongated uplifts form in the overstepping zones between segments, indicating restraining bends. Upward, in Upper Ordovician (T_7^0), the SHB-5 fault continues to develop with wider, longer overstepping zones (Fig. S5A). Near top Middle Devonian (T_6^0), the SHB-5 fault turns to a discrete, right-step, *en échelon* pattern (Fig. S5B), and switches to sinistral-slip (Liu et al., 2023). They become unrecognizable above Upper Permian (T_5^0).

Across SHB-5 fault, small fault offsets are present from Upper Neoproterozoic to Upper Permian (below T_5^0) (Fig. 2D). The fault contains a sub-vertical major fault below T_8^0 and two branches above T_8^0 (Liu et al., 2023). Two distinct domains exist within the flower structure: uplift in the lower half (e.g., T_7^4 and T_7^0), and subtle subsidence in the upper part (T_6^0). Small-scale growth strata can be inferred around T_7^0 based on thickness changes; however, the exact boundary is difficult to determine by naked eyes.

We interpret that these strike-slip faults sole into a regional detachment and apply the area-depth method here. The inferred detachment lies at ~10.5 km depth in the central section (G-G'), and shallows to ~10 km north- and southward (F-F', H-H').

5. Discussion

5.1 Timing of deformation

We plot the area-depth graphs for the five Tazhong sections and three Shunbei sections (Fig. 3). Strikingly, all graphs share a four-stage pattern:

(I) The pregrowth stage is hosted in Cambrian (T_9^0-T_8^0) and Precambrian (below T_9^0), characterized by linear area-depth relationships. The total shortening accommodated in the pregrowth strata ranges from 897-1805 m across Tazhong-2 thrust and 48-339 m across SHB-5 strike-slip fault (strike-slip component not considered), showing uneven distribution of finite strains.

(II) This growth stage began at T_8^0 (Cambrian-Ordovician boundary, ~485 Ma), as marked by changes in slope on area-depth graphs. The ratios of shortening to sedimentation rates ($d\bar{S}/dH$) varied with time. This stage ended in Late Devonian (shortly after T_6^0) across the Tazhong Uplift and northern SHB-5 faults, but in Early to Middle Devonian (before T_6^0) in central and southern SHB-5 fault. Despite local heterogeneities, the broadly coeval initiation and cessation of deformation in Tazhong-Shunbei indicate a common tectonic origin.

(III) A hiatus stage in deformation followed. It lasted from Middle to Late Devonian (around T_6^0) to Late Permian (T_5^0). It is marked by another segment of positive linear relation on each graph. Four best-fit lines can be projected to the original point within errors (Figs. 3A, B, D, H), whereas others are projected to various depths in Lower Paleozoic (Figs. 3C, E, F, G), indicating multiple detachments co-contributed to the deformation.

(IV) The second growth stage is characterized by a sharp descent of the area-depth curves throughout the entire Mesozoic (T_5^0 to T_3^0). This substantiates the aforementioned, newly, but vaguely interpreted, shallow set of growth strata. The shortening is minor, but non-zero. Despite local heterogeneities, the Mesozoic deformation is coeval, indicating, again, a common tectonic origin.

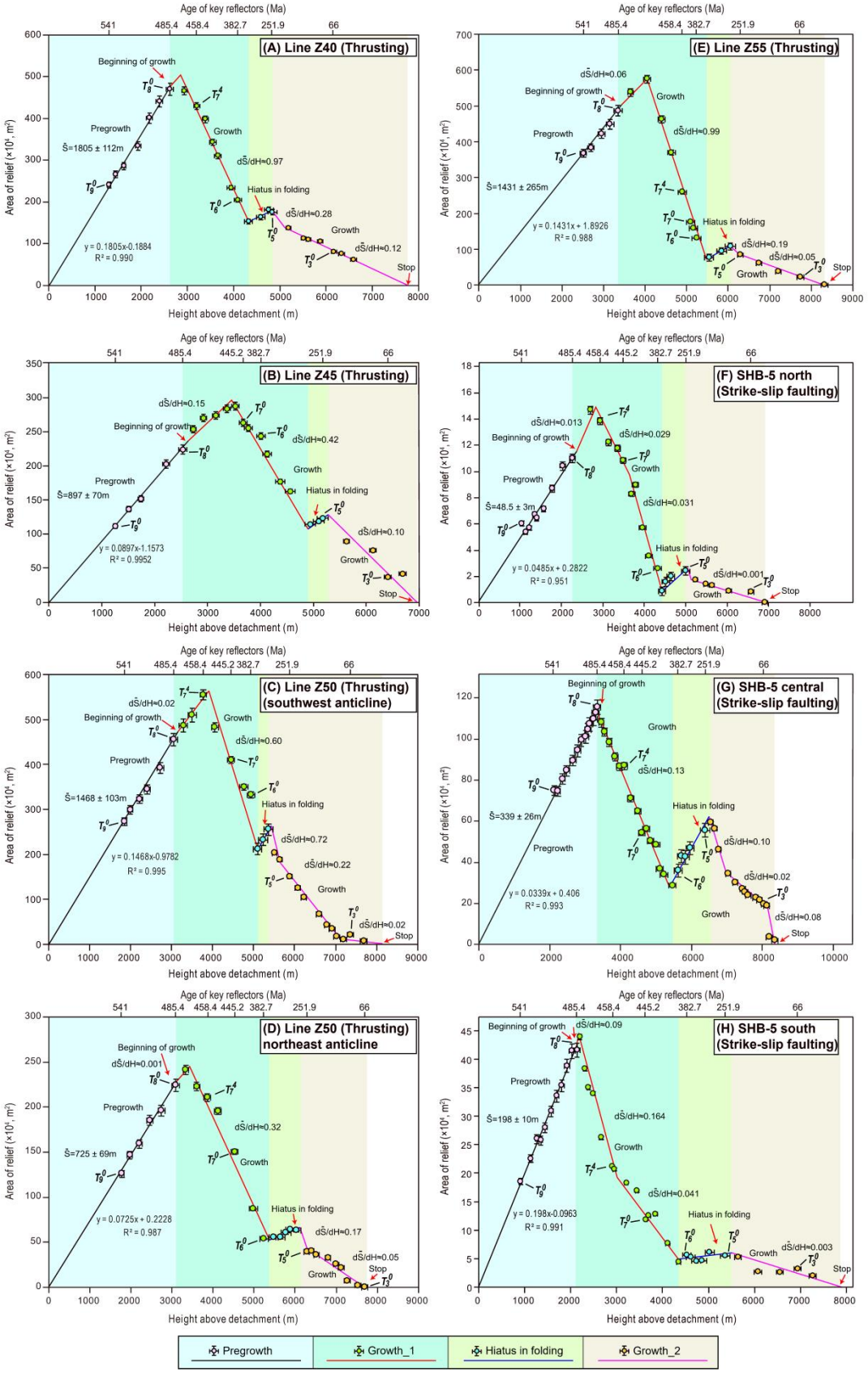
(A) Line Z40 (Thrusting)
(E) Line Z55 (Thrusting)
(B) Line Z45 (Thrusting)
(F) SHB-5 north (Strike-slip faulting)
(C) Line Z50 (Thrusting) (southwest anticline)
(G) SHB-5 central (Strike-slip faulting)
(D) Line Z50 (Thrusting) northeast anticline
(H) SHB-5 south (Strike-slip faulting)
Age of key reflectors (Ma)
Area of relief (×10⁴, m²)
Height above detachment (m)
Pregrowth
Growth_1
Hiatus in folding
Growth_2

243

Fig. 3. Area-depth graphs of thrusts and strike-slip faults in central Tarim Basin. (A)-(E) Fold-and-thrust structures in Tazhong Uplift. (F)-(H) North (F-F'), central (G-G'), and south (H-H') profiles across the SHB-5 fault in Shunbei. Approximate ages are marked on top of the graphs. S denotes shortening; H, height above detachment; d/dH, ratios of shortening rate to sedimentation rate.

5.2 Transpressional structural style

The inferred detachment depths fall in a narrow range of ca. 9.0~10.5 km. Considering the deformation ages, post-kinematic deposition, and lithospheric flexure (Yang & Liu, 2002), the regional detachment must be shallower in Paleo- and Mesozoic. We suggest that the detachment linkage mechanism (Bergen & Shaw, 2010) governs the growth, coalescence, and interaction of these faults in Tazhong-Shunbei, and a low-taper Coulomb wedge (Davis et al., 1983; Hubbard et al., 2010; Liu et al., 2020) characterizes the upper-crustal deformation that extends from the basin's margin to the interior.

The simultaneous deformation stages in Tazhong-Shunbei indicate a basin-wide, transpressional regime. Because SHB-5 fault's slip direction switches from dextral below to sinistral above T_6^0 (Liu et al., 2023) and the tectonic hiatus spans T_6^0 to T_5^0 (Fig. 4), SHB-5 must be dextral-slip during the first deformation stage and reactivated as a sinistral-slip fault in the second deformation stage. Collectively, an intense, dextral-transpressional strain field dominated the Tarim from Ordovician–Devonian, and a minor, sinistral-transpressional strain field existed in the Mesozoic.

5.3 Tectonics implications

We place the central Tarim in regional context to investigate the tectonic mechanisms and implications. For simplicity, all orientations are depicted in modern-day coordinates.

5.3.1 Early-Paleozoic deformation before Tarim recratonization

Although the timing of North Tarim - South Tarim amalgamation remains controversial (~1.9 Ga, Wu et al., 2020; 1.0-0.82 Ga, Xu et al., 2013; or 0.87-0.82 Ga, Zhao et al., 2021), the Central Tarim suture zone was reactivated in Early Paleozoic, leading to intense intra-continental deformation (Carroll et al., 1995; Yin & Nie, 1996; Guo et al., 2005; Qiu et al., 2019). This disqualifies the Tarim as a typical "craton" by then (Hoffman, 1988; Pearson et al., 2021).

The first stage of Phanerozoic deformation in central Tarim initiated by ~485 Ma (Cambrian-Ordovician boundary). This is ~25 Myr earlier than previously thought (Deng et al., 2019). It persisted for almost 100 Myr and waned by ~383 Ma (Middle Devonian). Because intra-continental shortening is generally driven by far-field compressional forces (Avouac & Tapponnier, 1993; Craddock & Pluijm, 1989), shortening in central Tarim can be an indicator for active Tarim margins, in the form of either Andean-type subduction or continental collision.

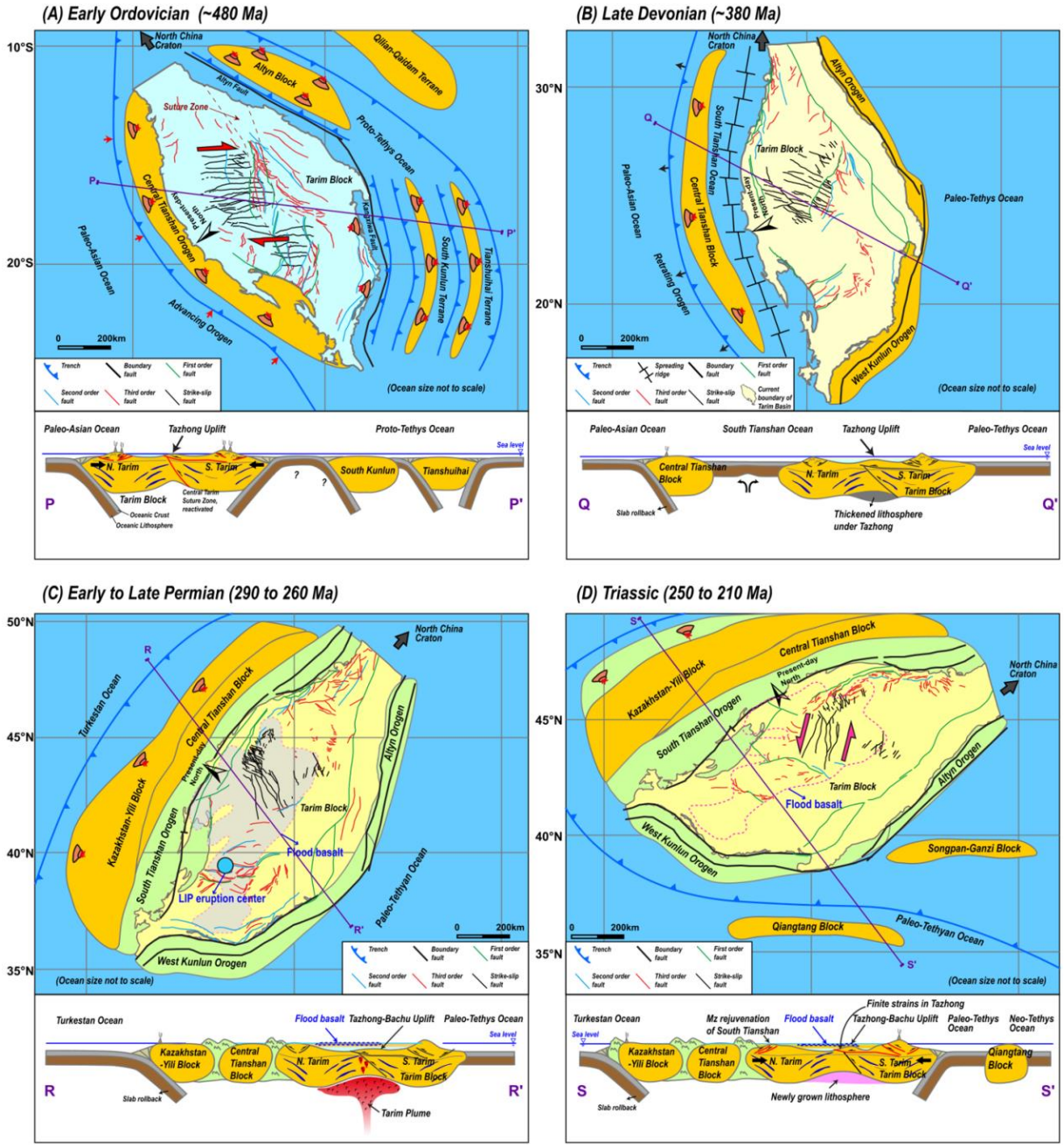

Fig. 4. Reconstructed paleogeographic and tectonic map of Tarim and surrounding plate boundaries and terranes (not to scale). (A) Early Ordovician (~480 Ma), highlighting the active Tarim margins as the Proto-Tethys and the Paleo-Asian Oceans are subducting underneath the Tarim block. Ordovician-aged faults are marked in red. (B) Late Devonian (~380 Ma), highlighting the formation of passive Tarim margins and the cessation of interior deformation. Devonian-aged faults are marked in red. (C) Early to Late Permian (ca. 290-260 Ma), highlighting the closure of South Tianshan Ocean and the Tarim LIP. Permian-aged faults are marked in red. (D) Triassic (ca. 250-210 Ma), showing the minor deformation in central Tarim. Triassic-aged faults are shown in red. The plate tectonic configurations are adapted from (Han et al., 2016). Extent of the Tarim LIP from (Xu et al., 2020).

Both the northern and southern Tarim margins were passive in Late Neoproterozoic-Early Cambrian (Cocks & Torsvik, 2013; Zhao et al., 2018). For Ordovician tectonics, it is debated whether the southern Tarim margin is passive (Matte et al., 1996) or active (Zhu et al., 2018). Our results independently corroborate the establishment of Andean-type southern Tarim margin with northward-subducting Proto-Tethyan Oytag-Kudi Ocean by the end of Cambrian. This is compatible with the Cambrian-Silurian (502-428 Ma) subduction-derived granitoids in southwestern Tarim (Yuan et al., 2002; Cui et al., 2007; Wang et al., 2020; Xu et al., 2020) and the northward subduction of Proto-Tethys Ocean since 530-520 Ma further to the east (J. Yao et al., 2021; Fu et al., 2022) (Fig. 4A).

The northern Tarim margin also played a critical role. Southward subduction of the Paleo-Asian Ocean initiated by ~500 Ma, inverting this passive margin to active (Carroll et al., 1995; Han et al., 2016; Windley et al., 1990). An advancing accretionary orogenesis dominated during ~500-400 Ma, causing subduction erosion and thickened crust (Cawood et al., 2009; Ge et al., 2014; Han et al., 2016). This facilitated the protracted (~100 Myr) transpression across the Tarim.

As the accretionary orogenesis switched from advancing to retreating at ~400 Ma (Early Devonian), crustal extension emerged in northern Tarim (Han et al., 2015, 2016; Wang et al., 2018) (Fig. 4B). To the south, the Paleo-Tethys Ocean also formed in Early–Middle Devonian, detaching the Tarim from East Gondwana (Han et al., 2016; Metcalfe, 2021). Consequently, the Early-Paleozoic intra-continental deformation is terminated.

5.3.2. Deformation hiatus (Late Devonian–Late Permian) and plume-lithosphere interactions

While the beginning of the hiatus stage (Late Devonian) is consistent with the resumption of passive Tarim margins (Han & Zhao, 2018), why intra-continental deformation is absent during the Tarim-Central Tianshan collision needs to be explained.

The key lies in plume-plate interactions (Fig. 4C). The long-lived Tarim plume generated a seamount chain in the South Tianshan Ocean during 425-330 Ma (Wan et al., 2020). As the the Tarim collided with the Central Tianshan–Yili block at ~325-310 Ma (Gao et al., 2011), the plume head may have been suppressed by the subducting slabs (Han & Zhao, 2018). It then penetrated the slab at ca. 300 Ma, interrupted the continental collision, and restricted surface uplift (Han & Zhao, 2018). Such a plume-modified collisional orogeny would not gain much gravitational potential energy and barely increase the compressive deviatoric stresses in the adjacent basin (Molnar & Lyon-Caen, 1988). Therefore, collision-induced deformation is absent in central Tarim.

In the following plume-lithosphere interactions (e.g., Xu et al., 2014), intraplate magmatism migrated from the thicker interior to thinner zones in and around the Tarim block, indicating lateral flow and accumulation of the buoyant, depleted, plume-derived melt residues into the thin lithospheric trap (Sleep, 1997). This process further caused melt-depletion and increased the viscosity in the southwestern Tarim mantle lithosphere (Deng et al., 2017). Cooling of the plume-derived melt residues marks the beginning of Tarim plume-driven recratonization (Xu et al., 2023).

338

339 *5.3.3 Mesozoic deformation during Tarim recratonization*

340 Mesozoic deformation, albeit small, exists in central Tarim. In contrast, this area
341 experienced no internal, basement-involved deformation in Cenozoic. This demonstrates that
342 Tarim did not become a stable craton in Permian. Instead, it continuously accommodated finite
343 strains in Mesozoic while the plume-welded lithosphere cools and strengthens.

344 The Tarim has been locked within the Asian continent since Mesozoic. Multiple oceans
345 have been consumed, including the Paleo-, Meso-, and Neo-Tethys Oceans that accreted multiple
346 terranes and raised the Tibetan Plateau (Kapp & DeCelles, 2019; Metcalfe, 2021; Murphy et al.,
347 1997; Yin & Harrison, 2000) (Fig. 4D). As a far-field response, the West Kunlun and Tianshan
348 Mountains underwent rejuvenation and uplift from Late Permian to Cretaceous (Cowgill et al.,
349 2003; Dumitru et al., 2001; Hendrix et al., 1992; Robinson et al., 2004). The Mesozoic finite
350 strain in central Tarim is stemmed from the continuous plate convergence.

351 A similar scenario happened in North America, where a plume interacted with the
352 Midcontinent Rift and produced the Keweenaw LIP at 1110-1083 Ma, followed by the inversion
353 of the rift that lasted until ca. 980 Ma during the Grenville orogeny (Gunawardana et al., 2022;
354 Hodgin et al., 2022; Stein et al., 2015). Hence, the southern Laurentia supercraton is finally
355 welded together at least 100 Myr after the rift's failure and the plume's cessation. While the
356 Midcontinent Rift example may give a minimum limit, our study from the Tarim basin offers an
357 independent, and complete, constraint on the timescale of plume-driven recratonization process.
358 Like Rome, a plume-welded craton was not built in a day; it could take ~200 Myr for such a
359 process to fully achieve.

360

361 **6. Conclusions**

362 (1) Area-depth method in seismic interpretation is useful to unravel the timing and
363 magnitude of deformation at sub-seismic resolution. It can be applied to strike-slip faults if a
364 regional detachment and syn-kinematic deposition are present.

365 (2) The thrust faults in Tazhong and strike-slip faults in Shunbei of central Tarim Basin
366 share a highly similar history, including an early stage of intense, dextral-transpressional
367 deformation in Earliest Ordovician-Middle Devonian, and a younger stage of minor, sinistral-
368 transpressional deformation throughout the Mesozoic. Both deformation stages are driven by
369 plate convergence surrounding Tarim.

370 (3) The newly-discovered Mesozoic deformation yields an unprecedented record of
371 continental deformation during the plume-driven recratonization as the lithosphere was cooling
372 and solidifying. The timescale of plume-driven recratonization is ~200 Myr.

373

374

375 **Acknowledgments**

376 We are grateful to Profs. An Yin and Timothy Kusky for providing constructive
377 comments on an early draft. This study is funded by Science Fund for Creative Research Groups

of National Natural Science Foundation of China (41821002), Strategic Priority Research Program of Chinese Academy of Sciences (XDA14010301), National Natural Science Foundation of China (41702138, 41702198), and Governor's University Research Initiative Fund from the State of Texas. The authors declare that they have no financial conflicts of interests.

Open Research

All data can be accessed in Supplementary Materials.

References

Avouac, J.-P., & Tapponnier, P. (1993). Kinematic model of active deformation in central Asia. *Geophysical Research Letters*, *20*(10), 895–898. https://doi.org/10.1029/93GL00128

Bergen, K. J., & Shaw, J. H. (2010). Displacement profiles and displacement-length scaling relationships of thrust faults constrained by seismic-reflection data. *GSA Bulletin*, *122*(7–8), 1209–1219. https://doi.org/10.1130/B26373.1

Carroll, A. R., Graham, S. A., Hendrix, M. S., Ying, D., & Zhou, D. (1995). Late Paleozoic tectonic amalgamation of northwestern China: Sedimentary record of the northern Tarim, northwestern Turpan, and southern Junggar Basins. *GSA Bulletin*, *107*(5), 571–594. https://doi.org/10.1130/0016-7606(1995)107<0571:LPTAON>2.3.CO;2

Cawood Peter A., Kröner Alfred, Collins William J., Kusky Timothy M., Mooney Walter D., & Windley Brian F. (2009). Accretionary orogens through Earth history. *Geological Society, London, Special Publications*, *318*(1), 1–36. https://doi.org/10.1144/SP318.1

Cocks, L. R. M., & Torsvik, T. H. (2013). The dynamic evolution of the Palaeozoic geography of eastern Asia. *Earth-Science Reviews*, *117*, 40–79. https://doi.org/10.1016/j.earscirev.2012.12.001

Cowgill, E., Yin, A., Harrison, T. M., & Xiao-Feng, W. (2003). Reconstruction of the Altyn Tagh fault based on U-Pb geochronology: Role of back thrusts, mantle sutures, and heterogeneous crustal strength in forming the Tibetan Plateau. *Journal of Geophysical Research: Solid Earth*, *108*(B7). https://doi.org/10.1029/2002JB002080

Craddock, J. P., & Pluijm, B. A. van der. (1989). Late Paleozoic deformation of the cratonic carbonate cover of eastern North America. *Geology*, *17*(5), 416–419. https://doi.org/10.1130/0091-7613(1989)017<0416:LPDOTC>2.3.CO;2

Cui, J. T., Wang, J. C., Bian, X. W., Zhu, H. P., Luo, Q. Z., Yang, K. J., & Wang, M. C. (2007). Zircon SHRIMP U-Pb dating of Early Paleozoic granite in the Menggubao-Pushou area on the northern side of Kangxiwar, West Kunlun. *Geological Bulletin of China*, *26*, 710–719.

Davis, D., Suppe, J., & Dahlen, F. A. (1983). Mechanics of fold-and-thrust belts and accretionary wedges. *Journal of Geophysical Research: Solid Earth*, *88*(B2), 1153–1172. https://doi.org/10.1029/JB088iB02p01153

Deng, S., Li, H., Zhang, Z., Zhang, J., & Yang, X. (2019). Structural characterization of intracratonic strike-slip faults in the central Tarim Basin. *AAPG Bulletin*, *103*(1), 109–137. https://doi.org/10.1306/06071817354

Deng, Y., Levandowski, W., & Kusky, T. (2017). Lithospheric density structure beneath the Tarim basin and surroundings, northwestern China, from the joint inversion of gravity and topography. *Earth and Planetary Science Letters*, *460*, 244–254. https://doi.org/10.1016/j.epsl.2016.10.051

Dumitru, T. A., Zhou, D., Chang, E. Z., Graham, S. A., Hendrix, M. S., Sobel, E. R., & Carroll, A. R. (2001). Uplift, exhumation, and deformation in the Chinese Tian Shan. *Memoirs-Geological Society of America*, 71–100.

Epard, J.-L., & Groshong, R. H., Jr. (1993). Excess Area and Depth to Detachment. *AAPG Bulletin*, *77*(8), 1291–1302. https://doi.org/10.1306/BDFF8E66-1718-11D7-8645000102C1865D

Fu, D., Huang, B., Johnson, T. E., Wilde, S. A., Jourdan, F., Polat, A., et al. (2022). Boninitic blueschists record subduction initiation and subsequent accretion of an arc–forearc in the northeast Proto-Tethys Ocean. *Geology*, *50*(1), 10–15. https://doi.org/10.1130/G49457.1

Gao, J., Klemd, R., Qian, Q., Zhang, X., Li, J., Jiang, T., & Yang, Y. (2011). The collision between the Yili and Tarim blocks of the Southwestern Altaids: Geochemical and age constraints of a leucogranite dike crosscutting the HP–LT metamorphic belt in the Chinese Tianshan Orogen. *Tectonophysics*, *499*(1), 118–131. https://doi.org/10.1016/j.tecto.2011.01.001

Ge, R., Zhu, W., Wilde, S. A., He, J., Cui, X., Wang, X., & Bihai, Z. (2014). Neoproterozoic to Paleozoic long-lived accretionary orogeny in the northern Tarim Craton. *Tectonics*, *33*(3), 302–329. https://doi.org/10.1002/2013TC003501

Gonzalez-Mieres, R., & Suppe, J. (2006). Relief and shortening in detachment folds. *Journal of Structural Geology*, *28*(10), 1785–1807.

Gonzalez-Mieres, R., & Suppe, J. (2011). Shortening Histories in Active Detachment Folds Based on Area-of-relief Methods. In K. McClay, J. Shaw, & J. Suppe (Eds.), *Thrust Fault-Related Folding* (Vol. 94, pp. 39–67). American Association of Petroleum Geologists. https://doi.org/10.1306/13251332M943428

Groshong, R. H., & Epard, J.-L. (1994). The role of strain in area-constant detachment folding. *Journal of Structural Geology*, *16*(5), 613–618. https://doi.org/10.1016/0191-8141(94)90113-9

Guo, Z.-J., Yin, A., Robinson, A., & Jia, C.-Z. (2005). Geochronology and geochemistry of deep-drill-core samples from the basement of the central Tarim basin. *Journal of Asian Earth Sciences*, *25*(1), 45–56.

Han, Y., & Zhao, G. (2018). Final amalgamation of the Tianshan and Junggar orogenic collage in the southwestern Central Asian Orogenic Belt: Constraints on the closure of the Paleo-Asian Ocean. *Reconstruction of East Asian Continental Blocks in Pangea*, *186*, 129–152. https://doi.org/10.1016/j.earscirev.2017.09.012

Han, Y., Zhao, G., Sun, M., Eizenhöfer, P. R., Hou, W., Zhang, X., et al. (2015). Paleozoic accretionary orogenesis in the Paleo-Asian Ocean: Insights from detrital zircons from Silurian to Carboniferous strata at the northwestern margin of the Tarim Craton. *Tectonics*, *34*(2), 334–351. https://doi.org/10.1002/2014TC003668

Han, Y., Zhao, G., Cawood, P. A., Sun, M., Eizenhöfer, P. R., Hou, W., et al. (2016). Tarim and North China cratons linked to northern Gondwana through switching accretionary tectonics and collisional orogenesis. *Geology*, *44*(2), 95–98. https://doi.org/10.1130/G37399.1

Hendrix, M. S., Graham, S. A., Carroll, A. R., Sobel, E. R., McKnight, C. L., Schulein, B. J., & Wang, Z. X. (1992). Sedimentary record and climatic implications of recurrent deformation in the Tian Shan: Evidence from Mesozoic strata of the north Tarim, south Junggar, and Turpan basins, northwest China. *GSA Bulletin*, *104*(1), 53–79. https://doi.org/10.1130/0016-7606(1992)104<0053:SRACIO>2.3.CO;2

Hodgin, E. B., Swanson-Hysell, N. L., DeGraff, J. M., Kylander-Clark, A. R. C., Schmitz, M. D., Turner, A. C., et al. (2022). Final inversion of the Midcontinent Rift during the Rigolet Phase of the Grenvillian Orogeny. *Geology*, *50*(5), 547–551. https://doi.org/10.1130/G49439.1

Hoffman, P. F. (1988). United Plates of America, The Birth of a Craton: Early Proterozoic Assembly and Growth of Laurentia. *Annual Review of Earth and Planetary Sciences*, *16*(1), 543–603. https://doi.org/10.1146/annurev.ea.16.050188.002551

Huang, B., Yan, Y., Piper, J. D. A., Zhang, D., Yi, Z., Yu, S., & Zhou, T. (2018). Paleomagnetic constraints on the paleogeography of the East Asian blocks during Late Paleozoic and Early Mesozoic times. *Reconstruction of East Asian Continental Blocks in Pangea*, *186*, 8–36. https://doi.org/10.1016/j.earscirev.2018.02.004

Hubbard, J., Shaw, J. H., & Klinger, Y. (2010). Structural Setting of the 2008 Mw 7.9 Wenchuan, China, Earthquake. *Bulletin of the Seismological Society of America*, *100*(5B), 2713–2735. https://doi.org/10.1785/0120090341

Kapp, P., & DeCelles, P. G. (2019). Mesozoic–Cenozoic geological evolution of the Himalayan-Tibetan orogen and working tectonic hypotheses. *American Journal of Science*, *319*(3), 159. https://doi.org/10.2475/03.2019.01

Koulakov, I. (2011). High-frequency P and S velocity anomalies in the upper mantle beneath Asia from inversion of worldwide traveltime data. *Journal of Geophysical Research: Solid Earth*, *116*(B4). https://doi.org/10.1029/2010JB007938

Lee, C.-T. A., Luffi, P., & Chin, E. J. (2011). Building and Destroying Continental Mantle. *Annual Review of Earth and Planetary Sciences*, *39*(1), 59–90. https://doi.org/10.1146/annurev-earth-040610-133505

Li, Z. X., Li, X. H., Kinny, P. D., Wang, J., Zhang, S., & Zhou, H. (2003). Geochronology of Neoproterozoic syn-rift magmatism in the Yangtze Craton, South China and correlations with other continents: evidence for a mantle superplume that broke up Rodinia. *Precambrian Tectonics of East Asia and Relevance to Supercontintent Evolution*, *122*(1), 85–109. https://doi.org/10.1016/S0301-9268(02)00208-5

Liu, J., Pearson, D. G., Wang, L. H., Mather, K. A., Kjarsgaard, B. A., Schaeffer, A. J., et al. (2021). Plume-driven recratonization of deep continental lithospheric mantle. *Nature*, *592*(7856), 732–736. https://doi.org/10.1038/s41586-021-03395-5

Liu, Yiduo, Tan, X., Ye, Y., Zhou, C., Lu, R., Murphy, M. A., et al. (2020). Role of erosion in creating thrust recesses in a critical-taper wedge: An example from Eastern Tibet. *Earth and Planetary Science Letters*, *540*, 116270. https://doi.org/10.1016/j.epsl.2020.116270

Liu, Yin, Suppe, J., Cao, Y., Hao, F., Liu, Y., Wang, X., et al. (2023). Linkage and formation of strike-slip faults in deep basins and the implications for petroleum accumulation: A case study from the Shunbei area of the Tarim Basin, China. *AAPG Bulletin*, *107*(2), 331–355. https://doi.org/10.1306/11142220110

Matte, Ph., Tapponnier, P., Arnaud, N., Bourjot, L., Avouac, J. P., Vidal, Ph., et al. (1996). Tectonics of Western Tibet, between the Tarim and the Indus. *Earth and Planetary Science Letters*, *142*(3), 311–330. https://doi.org/10.1016/0012-821X(96)00086-6

Metcalfe, I. (2021). Multiple Tethyan ocean basins and orogenic belts in Asia. *SPECIAL ISSUE: GR-100*, *100*, 87–130. https://doi.org/10.1016/j.gr.2021.01.012

Molnar, P., & Lyon-Caen, H. (1988). Some simple physical aspects of the support, structure, and evolution of mountain belts. In S. P. Clark Jr., B. C. Burchfiel, & J. Suppe (Eds.), *Processes in Continental Lithospheric Deformation* (Vol. 218, p. 0). Geological Society of America. https://doi.org/10.1130/SPE218-p179

Murphy, M. A., Yin, A., Harrison, T. M., Dürr, S. B., Z, C., Ryerson, F. J., et al. (1997). Did the Indo-Asian collision alone create the Tibetan plateau? *Geology*, *25*(8), 719–722. https://doi.org/10.1130/0091-7613(1997)025<0719:DTIACA>2.3.CO;2

Pearson, D. G., Scott, J. M., Liu, J., Schaeffer, A., Wang, L. H., van Hunen, J., et al. (2021). Deep continental roots and cratons. *Nature*, *596*(7871), 199–210. https://doi.org/10.1038/s41586-021-03600-5

Qiu, H., Deng, S., Cao, Z., Yin, T., & Zhang, Z. (2019). The evolution of the complex anticlinal belt with crosscutting strike-slip faults in the Central Tarim Basin, NW China. *Tectonics*, *38*(6), 2087–2113. https://doi.org/10.1029/2018TC005229

Robinson, A. C., Yin, A., Manning, C. E., Harrison, T. M., Zhang, S.-H., & Wang, X.-F. (2004). Tectonic evolution of the northeastern Pamir: Constraints from the northern portion of the Cenozoic Kongur Shan extensional system, western China. *GSA Bulletin*, *116*(7–8), 953–973. https://doi.org/10.1130/B25375.1

Safonova, I., Biske, G., Romer, R. L., Seltmann, R., Simonov, V., & Maruyama, S. (2016). Middle Paleozoic mafic magmatism and ocean plate stratigraphy of the South Tianshan, Kyrgyzstan. *Tectonic Evolution of the Qinling Orogen and Adjacent Orogenic Belts*, *30*, 236–256. https://doi.org/10.1016/j.gr.2015.03.006

Schlische, R. W., Groshong, R. H., Withjack, M. O., & Hidayah, T. N. (2014). Quantifying the geometry, displacements, and subresolution deformation in thrust-ramp anticlines with growth and erosion: From models to seismic-reflection profile. *Fluids and Structures in Fold and Thrust Belts with Recognition of the Work of David V. Wiltschko*, *69*, 304–319. https://doi.org/10.1016/j.jsg.2014.07.012

Shaw, J. H., Connors, C., & Suppe, J. (2005). *Seismic interpretation of contractional fault-related folds* (Vol. 53). Tulsa, Oklahoma, USA: The American Association of Petroleum Geologists.

Sleep, N. H. (1997). Lateral flow and ponding of starting plume material. *Journal of Geophysical Research: Solid Earth*, *102*(B5), 10001–10012. https://doi.org/10.1029/97JB00551

Stein, C. A., Kley, J., Stein, S., Hindle, D., & Keller, G. R. (2015). North America's Midcontinent Rift: When rift met LIP. *Geosphere*, *11*(5), 1607–1616. https://doi.org/10.1130/GES01183.1

Suppe, J. (1983). Geometry and kinematics of fault-bend folding. *American Journal of Science*, *283*(7), 684–721.

Suppe, J. (1985). *Principles of structural geology*. Prentice Hall.

Suppe, J. (2011). Mass Balance and Thrusting in Detachment Folds. In K. McClay, J. Shaw, & J. Suppe (Eds.), *Thrust Fault-Related Folding* (Vol. 94, pp. 21–37). American Association of Petroleum Geologists. https://doi.org/10.1306/13251331M94389

Suppe, J., & Medwedeff, D. (1990). Geometry and kinematics of fault-propagation folding. *Eclogae Geologicae Helvetiae*, *83*(3), 409–454.

Suppe, J., Chou, G. T., & Hook, S. C. (1992). Rates of folding and faulting determined from growth strata. In K. R. McClay (Ed.), *Thrust Tectonics* (pp. 105–121). Dordrecht: Springer Netherlands. https://doi.org/10.1007/978-94-011-3066-0_9

Suppe, J., Connors, C. D., & Zhang, Y. (2004). Shear Fault-bend Folding. In K. R. McClay (Ed.), *Thrust Tectonics and Hydrocarbon Systems* (Vol. 82, pp. 303–323). American Association of Petroleum Geologists. https://doi.org/10.1306/M82813C17

Vergés, J., Marzo, M., & Muñoz, J. A. (2002). Growth strata in foreland settings. *Sedimentary Geology*, *146*(1), 1–9. https://doi.org/10.1016/S0037-0738(01)00162-2

Wan, B., Wang, X., Liu, X., Cai, K., Xiao, W., & Mitchell, R. N. (2020). Long-lived seamount subduction in ancient orogens: Evidence from the Paleozoic South Tianshan. *Geology*, *49*(5), 531–535. https://doi.org/10.1130/G48547.1

Wang, X.-S., Klemd, R., Gao, J., Jiang, T., Li, J.-L., & Xue, S.-C. (2018). Final assembly of the southwestern Central Asian Orogenic Belt as constrained by the evolution of the South Tianshan Orogen: links with Gondwana and Pangea. *Journal of Geophysical Research: Solid Earth*, *123*(9), 7361–7388. https://doi.org/10.1029/2018JB015689

Windley, B. F., Allen, M. B., Zhang, C., Zhao, Z.-Y., & Wang, G.-R. (1990). Paleozoic accretion and Cenozoic redeformation of the Chinese Tien Shan Range, central Asia. *Geology*, *18*(2), 128–131. https://doi.org/10.1130/0091-7613(1990)018<0128:PAACRO>2.3.CO;2

Woodcock, N. H., & Fischer, M. (1986). Strike-slip duplexes. *Journal of Structural Geology*, *8*(7), 725–735. https://doi.org/10.1016/0191-8141(86)90021-0

Wu, G., Yang, S., Meert, J. G., Xiao, Y., Chen, Y., Wang, Z., & Li, X. (2020). Two phases of Paleoproterozoic orogenesis in the Tarim Craton: Implications for Columbia assembly. *Gondwana Research*, *83*, 201–216. https://doi.org/10.1016/j.gr.2020.02.009

Xiao, W., Windley, B. F., Hao, J., & Li, J. (2002). Arc-ophiolite obduction in the Western Kunlun Range (China): implications for the Palaeozoic evolution of central Asia. *Journal of the Geological Society*, *159*(5), 517–528. https://doi.org/10.1144/0016-764901-093

Xu, X., Zuza, A. V., Yin, A., Lin, X., Chen, H., & Yang, S. (2020). Permian plume-strengthened Tarim lithosphere controls the Cenozoic deformation pattern of the Himalayan-Tibetan orogen. *Geology*, *49*(1), 96–100. https://doi.org/10.1130/G47961.1

Xu, X., Chen, H., Zuza, A. V., Yin, A., Yu, P., Lin, X., et al. (2023). Phanerozoic cratonization by plume welding. *Geology*. https://doi.org/10.1130/G50615.1

Xu, Y.-G., Wei, X., Luo, Z.-Y., Liu, H.-Q., & Cao, J. (2014). The Early Permian Tarim Large Igneous Province: main characteristics and a plume incubation model. *Lithos*, *204*, 20–35.

Xu, Z.-Q., He, B.-Z., Zhang, C.-L., Zhang, J.-X., Wang, Z.-M., & Cai, Z.-H. (2013). Tectonic framework and crustal evolution of the Precambrian basement of the Tarim Block in NW China: New geochronological evidence from deep drilling samples. *Precambrian Research*, *235*, 150–162. https://doi.org/10.1016/j.precamres.2013.06.001

Yang, H., Wu, G., Kusky, T. M., Chen, Y., & Xiao, Y. (2018). Paleoproterozoic assembly of the North and South Tarim terranes: New insights from deep seismic profiles and Precambrian granite cores. *Precambrian Research*, *305*, 151–165. https://doi.org/10.1016/j.precamres.2017.11.015

Yang, Y., & Liu, M. (2002). Cenozoic deformation of the Tarim plate and the implications for mountain building in the Tibetan Plateau and the Tian Shan. *Tectonics*, *21*(6), 9–1. https://doi.org/10.1029/2001TC001300

Yao, J., Cawood, P. A., Zhao, G., Han, Y., Xia, X., Liu, Q., & Wang, P. (2021). Mariana-type ophiolites constrain the establishment of modern plate tectonic regime during Gondwana assembly. *Nature Communications*, *12*(1), 4189. https://doi.org/10.1038/s41467-021-24422-z

Yao, Z., He, G., Li, C.-F., & Dong, C. (2018). Sill geometry and emplacement controlled by a major disconformity in the Tarim Basin, China. *Earth and Planetary Science Letters*, *501*, 37–45. https://doi.org/10.1016/j.epsl.2018.08.026

Yin, A, & Nie, S. (1996). A Phanerozoic palinspastic reconstruction of China and its neighboring regions. In *The tectonic evolution of Asia* (pp. 442–485). Cambridge University New York.

Yin, A., & Harrison, T. M. (2000). Geologic evolution of the Himalayan-Tibetan orogen. *Annual Review of Earth and Planetary Sciences*, *28*(1), 211–280.

York, D., Evensen, N. M., Martínez, M. L., & De Basabe Delgado, J. (2004). Unified equations for the slope, intercept, and standard errors of the best straight line. *American Journal of Physics*, *72*(3), 367–375. https://doi.org/10.1119/1.1632486

Yu, Y., Tang, L., Yang, W., Huang, T., Qiu, N., & Li, W. (2014). Salt structures and hydrocarbon accumulations in the Tarim Basin, northwest China. *AAPG Bulletin*, *98*(1), 135–159. https://doi.org/10.1306/05301311156

Zhang, C.-L., Li, Z.-X., Li, X.-H., Xu, Y.-G., Zhou, G., & Ye, H.-M. (2010). A Permian large igneous province in Tarim and Central Asian orogenic belt, NW China: Results of a ca. 275 Ma mantle plume? *GSA Bulletin*, *122*(11–12), 2020–2040. https://doi.org/10.1130/B30007.1

Zhao, G., Wang, Y., Huang, B., Dong, Y., Li, S., Zhang, G., & Yu, S. (2018). Geological reconstructions of the East Asian blocks: From the breakup of Rodinia to the assembly of Pangea. *Reconstruction of East Asian Continental Blocks in Pangea*, *186*, 262–286. https://doi.org/10.1016/j.earscirev.2018.10.003

Zhao, P., He, J., Deng, C., Chen, Y., & Mitchell, R. N. (2021). Early Neoproterozoic (870–820 Ma) amalgamation of the Tarim craton (northwestern China) and the final assembly of Rodinia. *Geology*, *49*(11), 1277–1282. https://doi.org/10.1130/G48837.1

Zhu, J., Li, Q., Chen, X., Tang, H., Wang, Z., Chen, Y., et al. (2018). Geochemistry and petrogenesis of the early Palaeozoic appinite-granite complex in the Western Kunlun Orogenic Belt, NW China: implications for Palaeozoic tectonic evolution. *Geological Magazine*, *155*(8), 1641–1666. https://doi.org/10.1017/S0016756817000450

Figure 1. Location and geological background. (A) Tectonic map of Tarim block and surrounding regions. (B) Topography, major faults, and tectonic units in Tarim. (C) Fault systems in Tazhong-Shunbei. Base map shows the depth (in two-way traveltime) of top Middle Ordovician. White line denotes the 2-D seismic lines in Figs. 2A and S1. Red polygon marks the horizon slices in Figs. 2C and S3. Blue line marks the eight sections for area-depth analysis.

Figure 2. Seismic interpretation results and area-depth analyses. (A) Interpreted 2-D seismic profile A-A' on Line Z40 across Tazhong Uplift. Horizontal axis is common-depth-point. Vertical axis is two-way traveltime. Vertical exaggeration: ~3 times. (B) Area-depth analysis on depth-domain section a-a' within profile A-A'. (C) Horizontal slice of reflectors T_7^4 (top Middle Ordovician) in Shunbei. (D) Interpreted profile G-G' across SHB-5 fault in Shunbei. Vertical exaggeration: ~3.5 times. (E) Area-depth analysis on depth-domain profile G-G'. See Fig. 1C for locations.

Figure 3. Area-depth graphs of thrusts and strike-slip faults in central Tarim Basin. (A)-(E) Fold-and-thrust structures in Tazhong Uplift. (F)-(H) North (F-F'), central (G-G'), and south (H-H') profiles across the SHB-5 fault in Shunbei. Approximate ages are marked on top of the graphs. S denotes shortening; H, height above detachment; $d\bar{S}/dH$, ratios of shortening rate to sedimentation rate.

Figure 4. Reconstructed paleogeographic and tectonic map of Tarim and surrounding plate boundaries and terranes (not to scale). (A) Early Ordovician (~480 Ma), highlighting the active Tarim margins as the Proto-Tethys and the Paleo-Asian Oceans are subducting underneath the Tarim block. Ordovician-aged faults are marked in red. (B) Late Devonian (~380 Ma), highlighting the formation of passive Tarim margins and the cessation of interior deformation. Devonian-aged faults are marked in red. (C) Early to Late Permian (ca. 290-260 Ma), highlighting the closure of South Tianshan Ocean and the Tarim LIP. Permian-aged faults are marked in red. (D) Triassic (ca. 250-210 Ma), showing the minor deformation in central Tarim. Triassic-aged faults are shown in red. The plate tectonic configurations are adapted from (Han et al., 2016). Extent of the Tarim LIP from (Xu et al., 2020).

Figure 1.

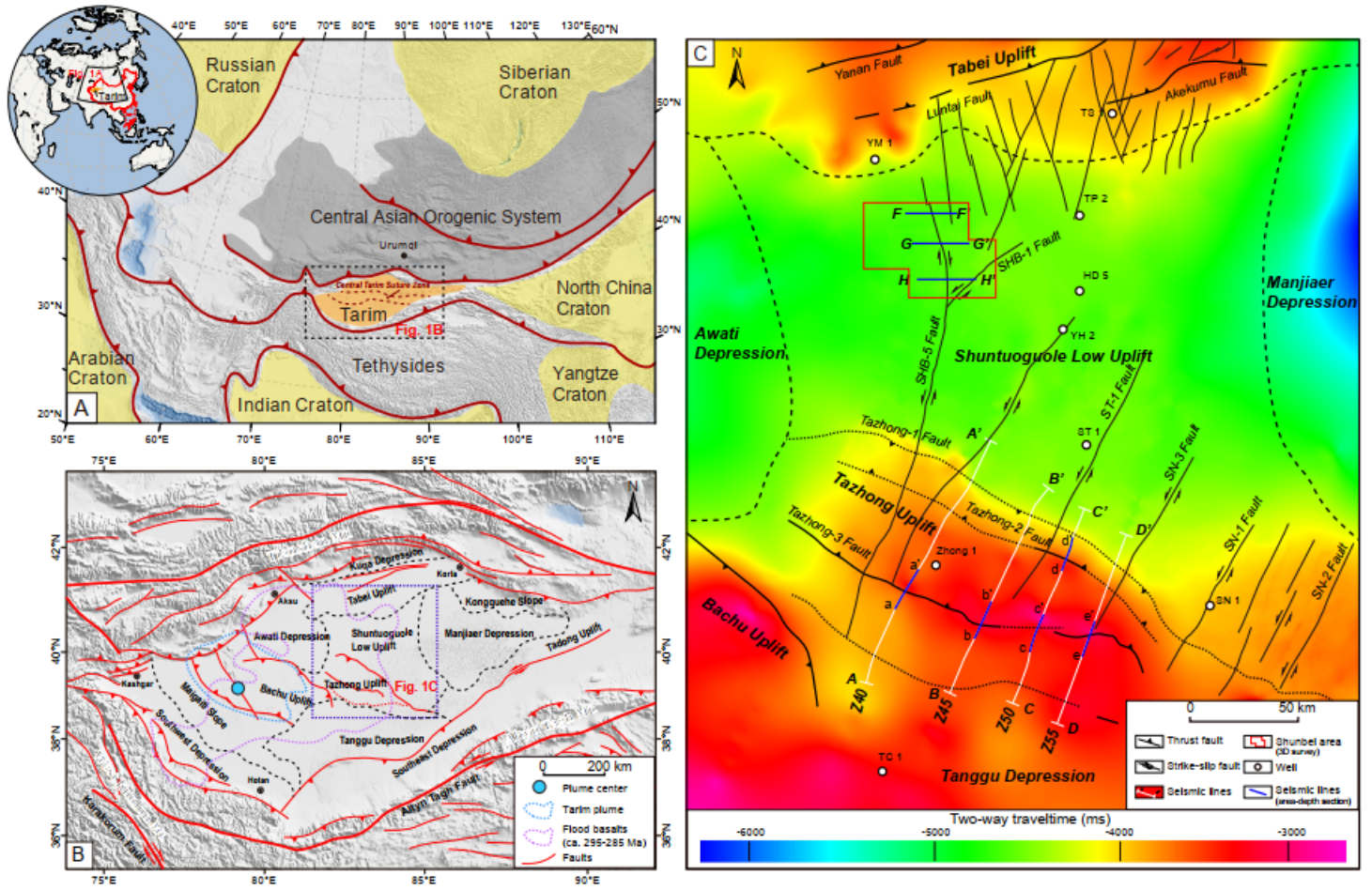
A
Russian Craton
Siberian Craton
Central Asian Orogenic System
Urumqi
Central Tarim Suture Zone
Tarim
Fig. 1B
North China Craton
Arabian Craton
Tethysides
Yangtze Craton
Indian Craton
B
Kuqa Depression
Karla
Akau
Tabei Uplift
Kongquehe Slope
Awati Depression
Shuntuoguole Low Uplift
Manjiaer Depression
Tadong Uplift
Kashgar
Bachu Uplift
Tazhong Uplift
Fig. 1C
Malgaili Slope
Southwest Depression
Tanggu Depression
Southeast Depression
Hotan
Aqtyn Tagh Fault
Karakorum Fault
0 200 km
Plume center
Tarim plume
Flood basalts (ca. 295-285 Ma)
Faults
C
Yanan Fault
Tabei Uplift
Luntai Fault
Akekumu Fault
YM 1
TB
TP 2
F
F'
G
G'
H
H'
SHB-1 Fault
HD 5
Manjiaer Depression
Awati Depression
YH 2
Shuntuoguole Low Uplift
SHB-5 Fault
ST-1 Fault
Tazhong-1 Fault
A'
ST 1
SN-3 Fault
B'
C'
D'
Tazhong Uplift
Tazhong-3 Fault
Tazhong-2 Fault
Zhong 1
SN-1 Fault
SN-2 Fault
SN 1
Bachu Uplift
A
B
C
D
Z40
Z45
Z50
Z55
TC 1
Tanggu Depression
0 50 km
Thrust fault
Strike-slip fault
Seismic lines
Shunbei area (3D survey)
Well
Seismic lines (cross-depth section)
Two-way traveltime (ms)
-6000
-5000
-4000
-3000

Figure 2.

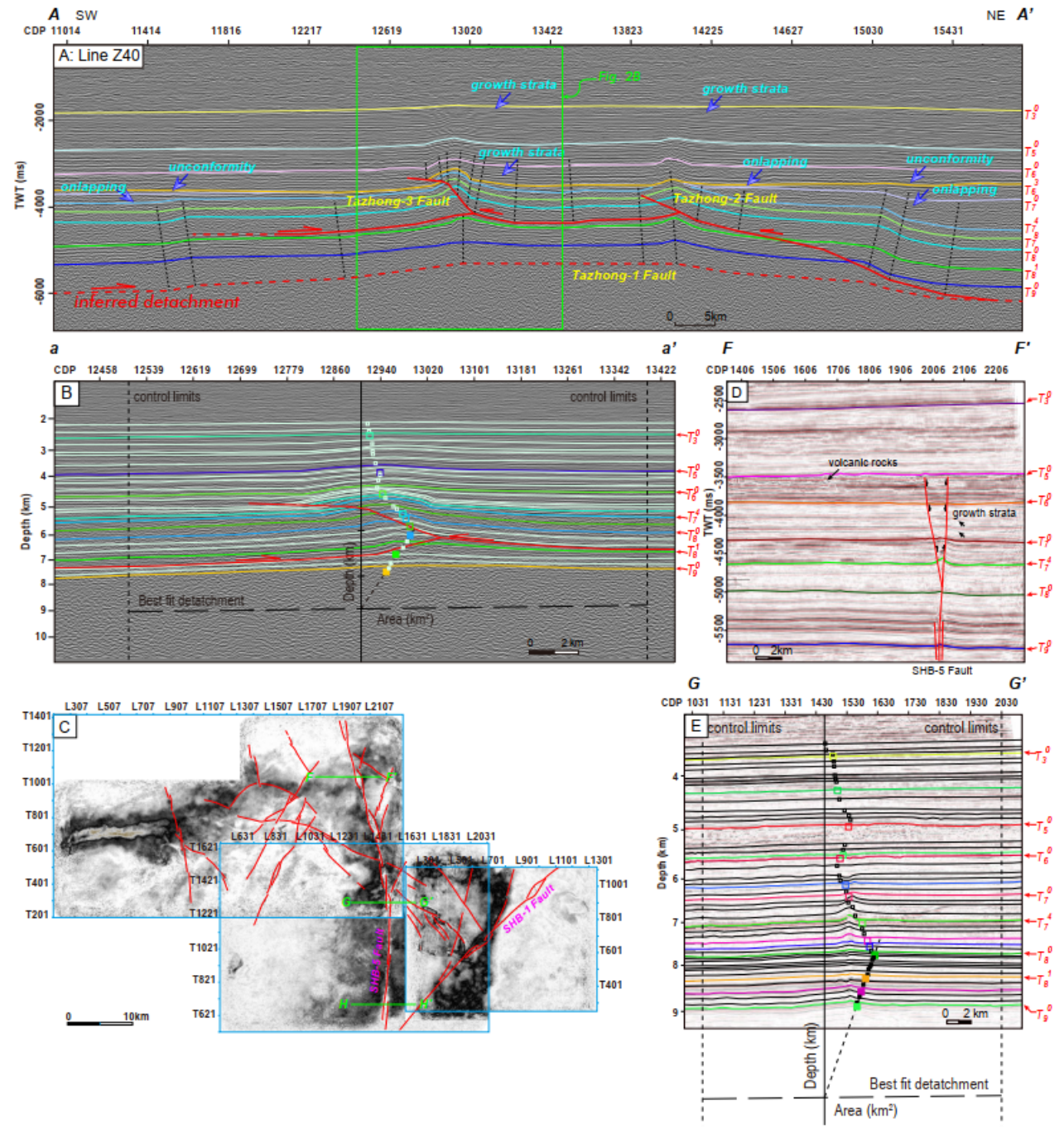
A
SW
NE
A'
CDP 11014 11414 11816 12217 12619 13020 13422 13823 14225 14627 15030 15431
A: Line Z40
growth strata
Fig. 3B
growth strata
growth strata
unconformity
onlapping
onlapping
unconformity
onlapping
Taizhong-3 Fault
Tazhong-2 Fault
Tazhong-1 Fault
inferred detachment
TWT (ms)
-2000
-4000
-6000
0 5km
a
a'
CDP 12458 12539 12619 12699 12779 12860 12940 13020 13101 13181 13261 13342 13422
B
control limits
control limits
Depth (km)
Best fit detatchment
Depth (km)
Area (km²)
0 2 km
F
F'
CDP 1406 1506 1606 1706 1806 1906 2006 2106 2206
D
volcanic rocks
growth strata
TWT (ms)
-2500
-3000
-3500
-4000
-4500
-5000
-5500
0 2km
SHB-5 Fault
G
G'
CDP 1031 1131 1231 1331 1430 1530 1630 1730 1830 1930 2030
E
control limits
control limits
Depth (km)
Best fit detatchment
Depth (km)
Area (km²)
0 2 km
L307 L507 L707 L907 L1107 L1307 L1507 L1707 L1907 L2107
C
T1401
T1201
T1001
T801
T601
T401
T201
L631 L831 L1031 L1231 L1431 L1631 L1831 L2031
T1621
T1421
T1221
T1021
T821
T621
L701 L901 L1101 L1301
T1001
T801
T601
T401
SHB-4 Fault
SHB-1 Fault
0 10km

Figure 3.

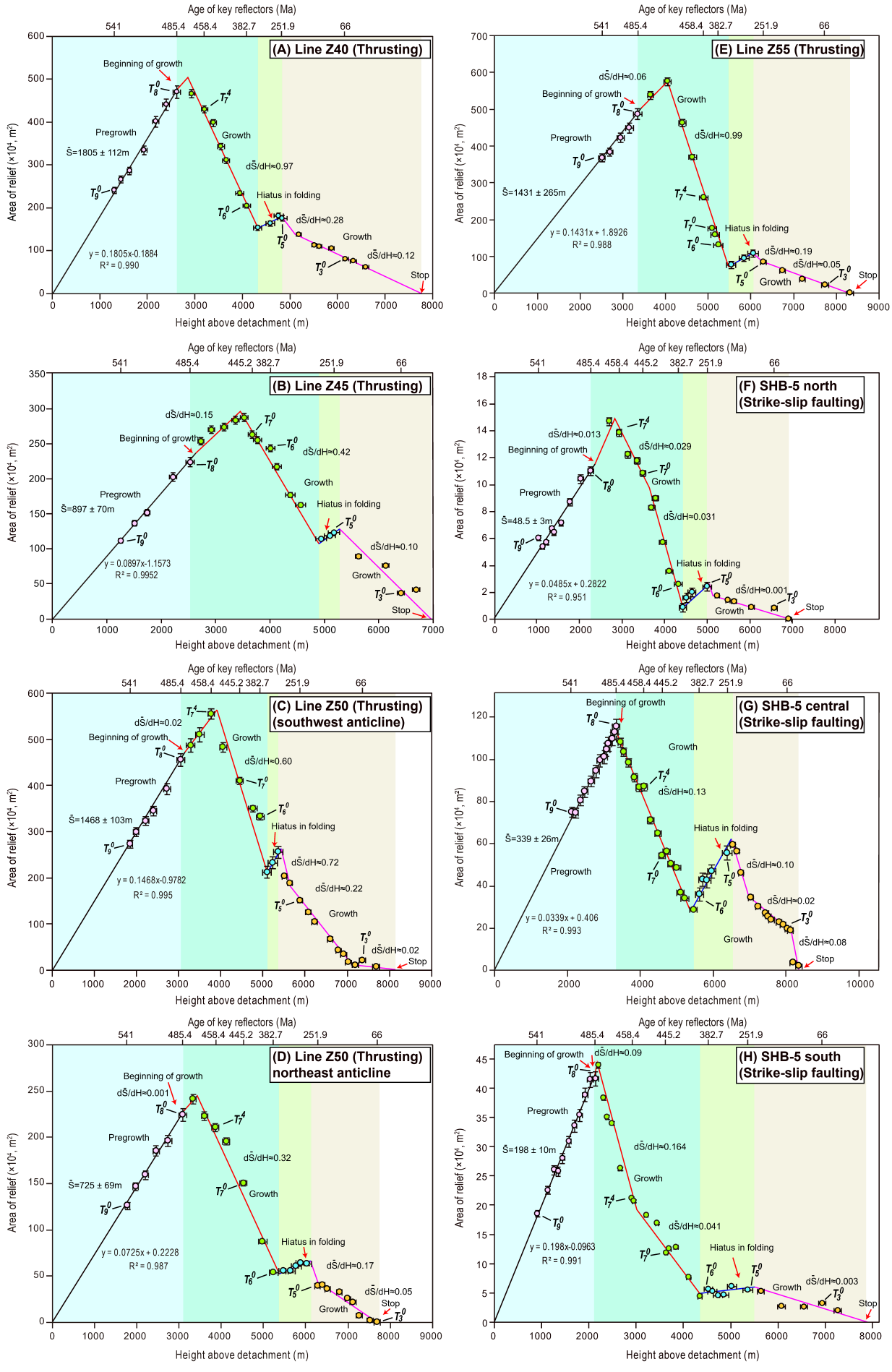
(A) Line Z40 (Thrusting)
(E) Line Z55 (Thrusting)
(B) Line Z45 (Thrusting)
(F) SHB-5 north (Strike-slip faulting)
(C) Line Z50 (Thrusting) (southwest anticline)
(G) SHB-5 central (Strike-slip faulting)
(D) Line Z50 (Thrusting) northeast anticline
(H) SHB-5 south (Strike-slip faulting)
Age of key reflectors (Ma)
Area of relief (×10⁴, m²)
Height above detachment (m)
Pregrowth
Growth_1
Hiatus in folding
Growth_2

Figure 4.

(A) Early Ordovician (~480 Ma)

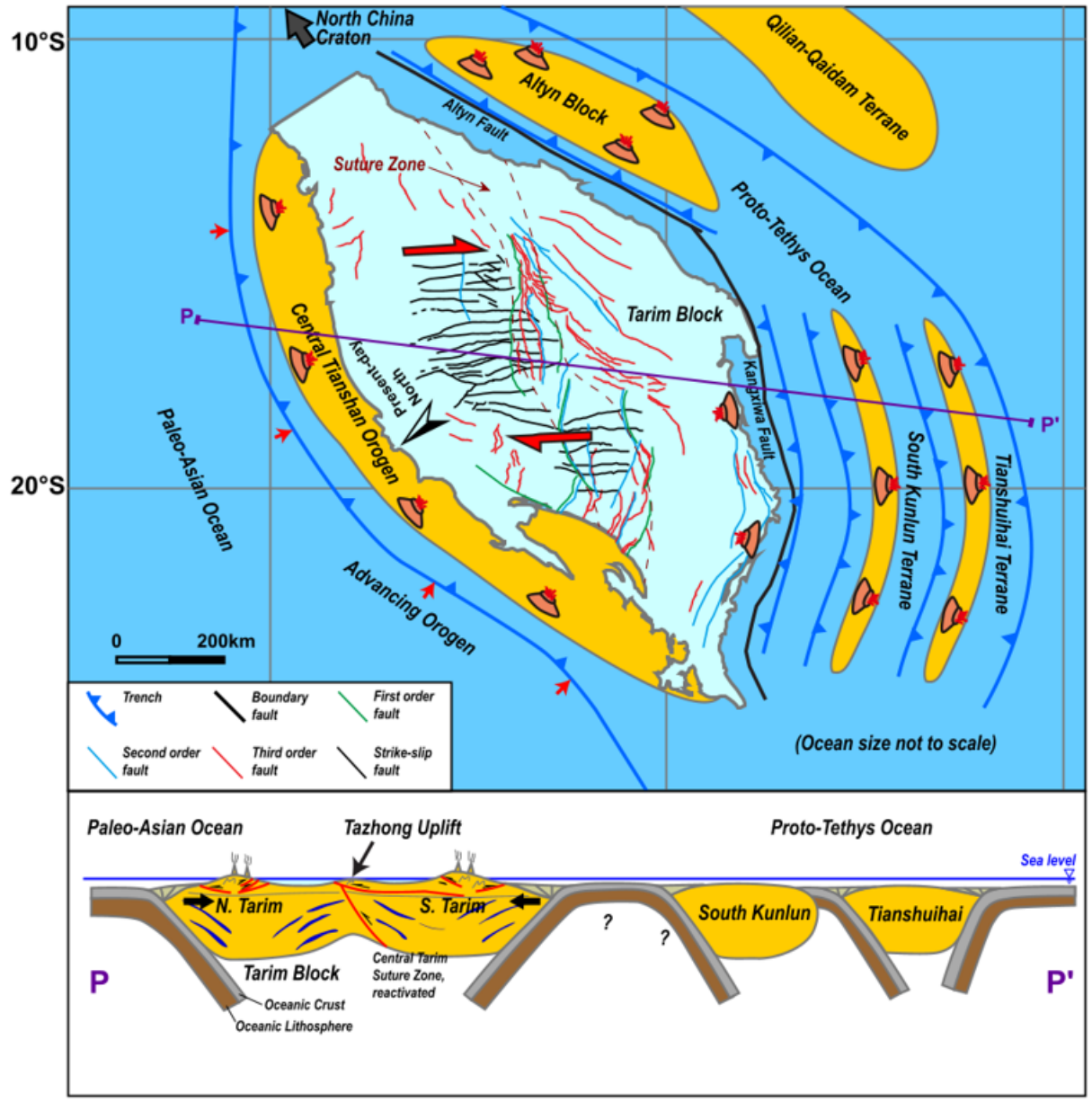

(B) Late Devonian (~380 Ma)

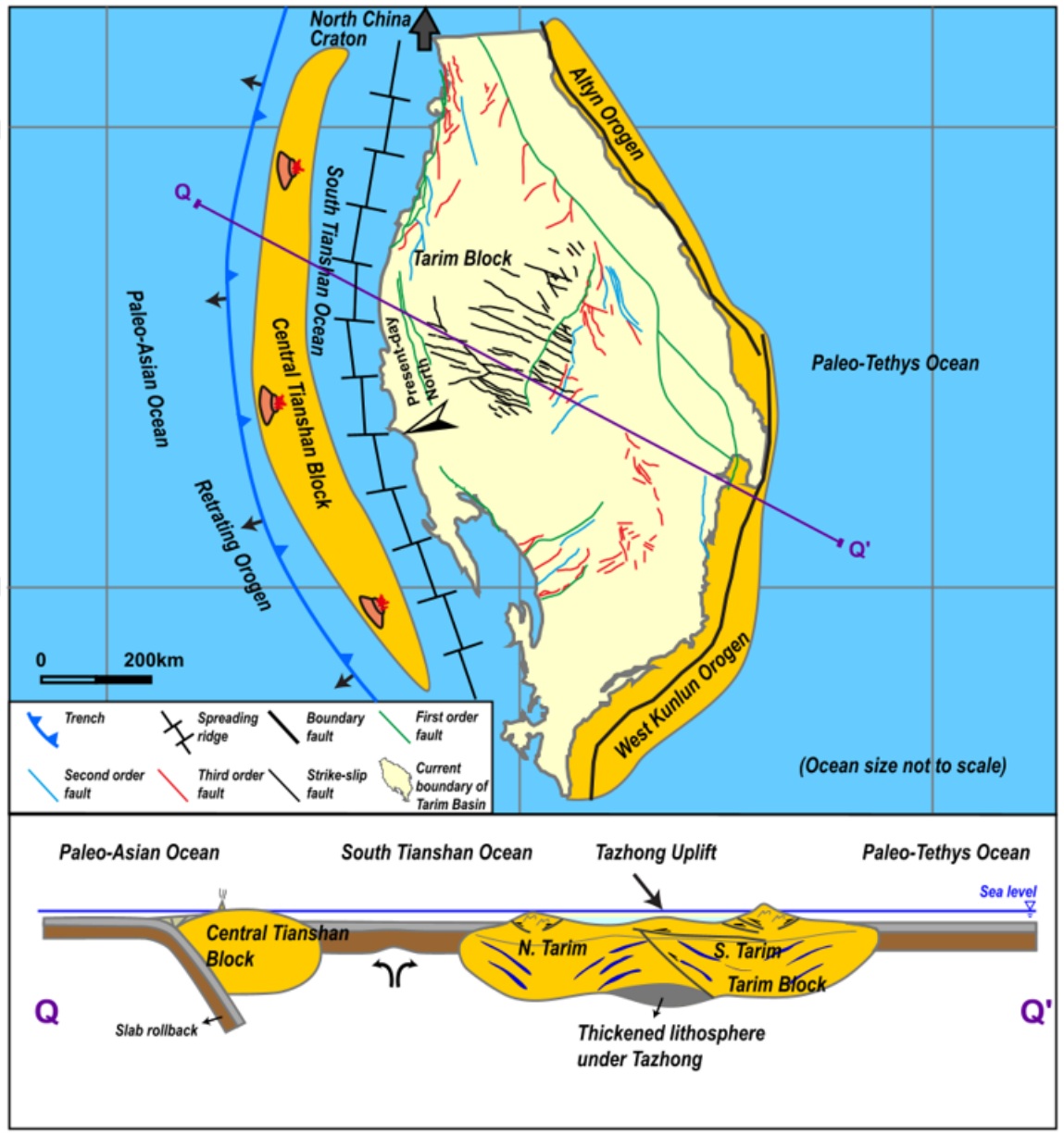

(C) Early to Late Permian (290 to 260 Ma)

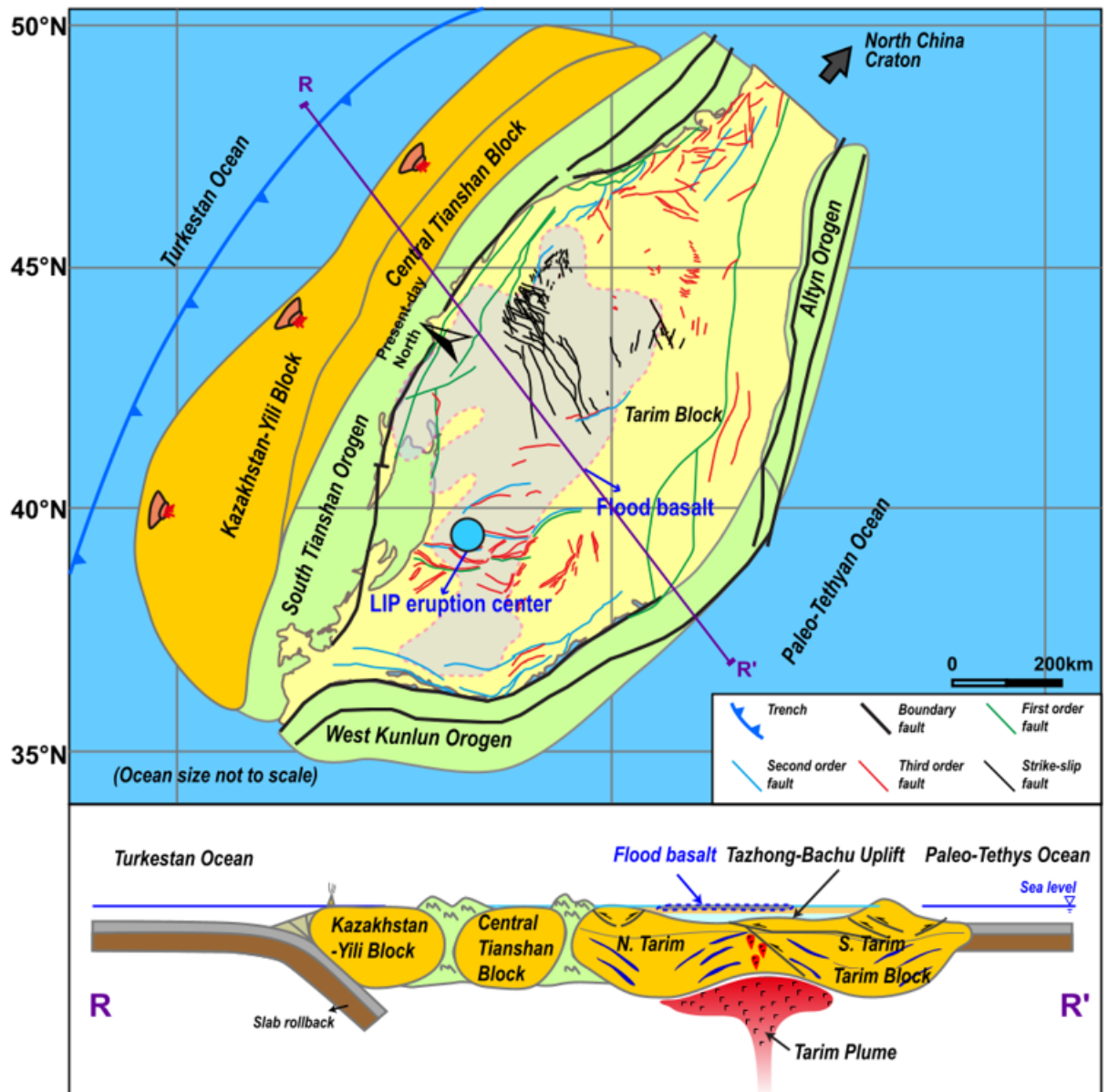

(D) Triassic (250 to 210 Ma)